Global and Planetary Change 259 (2026) 105360

Contents lists available at ScienceDirect

Global and Planetary Change

journal homepage: www.elsevier.com/locate/gloplacha

Research Article

Thermal and compositional state of the South African Cratonic Region from seismic and gravity models

Magdala Tesauro [a,b,*], Mikhail K. Kaban [c,d], Mohammad Youssof [e,f]

[a] Trieste University, Mathematics, Informatics, and Geosciences, Trieste, Italy
[b] Utrecht University, Earth Science Department, Utrecht, Netherlands
[c] Geophysical Center of the Russian Academy of Sciences, Moscow, Russia
[d] GFZ German Research Centre for Geosciences, Potsdam, Germany
[e] Niels Bohr Institute, University of Copenhagen, Copenhagen, Denmark
[f] GeoHazard Center, Saudi Geological Survey, Jeddah, Saudi Arabia

ARTICLE INFO

Editor: Sun Jimin

Keywords:
South Africa Cratons
Thermal model
Gravity anomalies
Compositional model
iron depletion

ABSTRACT

Tomographic models of seismic velocity perturbations provide valuable insights into the Earth's interior. Yet, because seismic velocities are primarily temperature-dependent, they mostly capture thermal anomalies. Combining them with gravity data enables a joint interpretation that can also account for compositional variations in the upper mantle beneath Precambrian cratons. The South African cratonic region is composed of the Archean Kaapvaal and Zimbabwe craton and, according to xenolith analysis, underlain by a heterogeneous upper mantle both in terms of temperature and composition.

To unravel the temperature and compositional anomalies with corresponding density variations and to link them to the tectonic history of that area, we apply an integrative technique based on a joint interpretation of the seismic tomography and gravity data. We combine a global shear seismic tomography model with an embedded high-resolution regional model and we invert it for temperature, assuming an initial composition, representative of a refertilized upper mantle. The composition and temperature of the upper mantle are iteratively changed, increasing progressively the amount of iron depletion, to fit the residual density, obtained from the joint inversion of the residual gravity and residual topography, and GOCE gravity gradients. The results show significant lithospheric compositional variations consistent with the tectonic history of the area. The most depleted lithosphere is located in the Southeastern Terrane of the Kaapvaal craton, at depth < 100 km, generating a temperature higher than $\sim$150 °C, with respect to that of a refertilized lithosphere.

1. Introduction

Earth's dynamics are responsible for the main lateral and in-depth thermo-physical variations of the lithosphere, which, as the outer shell of the solid Earth, is the layer where most natural resources (e.g., water and mineral resources) are located. Therefore, understanding the thermo-physical structure of the lithosphere is crucial for recognizing its exploitable potential. Most of the continental crust is of Precambrian age and composes the cratonic lithosphere that lack obvious short-term tectonic activity (Mooney, 2007). The cratons longevity and stability are related to the generally thick (> 200 km), cold, high viscous, and compositionally buoyant lithosphere (Jordan, 1978). However, several studies have already demonstrated that the cratonic lithosphere can be modified or even destroyed, mainly by interacting with melts and/or hydrothermal fluids, derived by several tectonic events, such as mantle plumes uprising, rifting and subduction zone formations (e.g., Lee et al., 2011; Sobolev et al., 2011; Kusky et al., 2014; Wang et al., 2015; Zhang et al., 2024). Among the others, the Wyoming craton has been destabilized by the combined effects of flat-slab subduction, small-scale convection, and hotspot activity (e.g., Dave and Li, 2016; Snyder et al., 2017), the lithosphere of the Tanzania craton has been significantly weakened by the impingement of a mantle plume (e.g., Weeraratne et al., 2003; Adams et al., 2012), and the North China Craton has been decratonized by the flat slab subduction, followed by a rollback of the Pacific plate during the Meso-Cenozoic (e.g., Zhu and Zheng, 2009; Wu et al., 2019). Furthermore, recent seismic tomography models produced evidence of a thinner lithosphere beneath some cratonic areas (e.g., Siberian Craton, Baltic Shield, African cratons) and demonstrated

* Corresponding author at: Trieste University, Mathematics, Informatics, and Geosciences, Trieste, Italy.
E-mail address: mtesauro@units.it (M. Tesauro).

https://doi.org/10.1016/j.gloplacha.2026.105360
Received 1 October 2025; Received in revised form 2 February 2026; Accepted 2 February 2026
Available online 3 February 2026

that the cratonic lithosphere has not been entirely preserved, but often eroded, especially along the cratons' edges, as an effect of several magmatic events (e.g., Bedle et al., 2021; Boyce et al., 2021; Celli et al., 2020; Legendre et al., 2012).

The African lithosphere is mostly of Precambrian age and thus includes several cratons, whose lithospheric velocity and thickness, in the last few decades have been progressively investigated with a major detail, mostly through seismic tomography studies (e.g., Sebai et al., 2006; Pasyanos and Nyblade, 2007; Begg et al., 2009; Fishwick, 2010; Youssof et al., 2015; Emry et al., 2019; Celli et al., 2020; Boyce et al., 2021). However, only in the last few years, some studies have focused on the thermo-compositional heterogeneities of the African lithosphere (Afonso et al., 2022; Finger et al., 2022). While temperatures can be deduced from the inversion of seismic velocities assuming a uniform composition, it is more challenging to derive temperatures that account for compositional variations. Indeed, analyzing xenoliths is the only direct approach that can be used for this purpose. However, these data are punctual and do not have a uniform coverage in space neither in time. The recent study of Afonso et al. (2022) followed a probabilistic joint inversion method, which uses types of geophysical data (e.g., seismic data, geoid and gravity anomalies, elevation, surface heat flow, and gravity gradients) to derive at the same time the lithospheric thermal and compositional field of the Central Africa. Finger et al. (2022), using a new model of Moho depth and data on crustal density structure of the entire African continent, together with global dynamic models, calculated residual topography and mantle gravity residuals. These were jointly inverted to derive residual densities, using temperatures from seismic tomography inversion, assuming a uniform composition, as constraints. The residual densities obtained were iteratively adjusted with a new composition, and the temperatures were progressively corrected accordingly. This approach yielded a consistent thermal and compositional model, reflecting density and Mg # variations of the African upper mantle.

In this study, we follow the same approach described in Finger et al. (2022) and other previous studies (e.g., Kaban et al., 2014a, 2014b; Tesauro et al., 2014; Tesauro et al., 2020), to obtain a thermo-compositional model of the upper mantle underneath the oldest Precambrian shield of southern Africa, better known as Kalahari Craton. In this area of interest, we took the advantage to use the regional seismic tomography models of Youssof et al. (2015), providing more details than global and continental models (e.g., Schaeffer and Lebedev, 2013; Emry et al., 2019; Celli et al., 2020; Boyce et al., 2021; van Herwaarden et al., 2023). In addition, we performed also a second type of inversion, which, besides the residual topography and mantle gravity residuals, includes the vertical gravity gradients (g_z) of GOCE. Indeed, this additional field should improve the reliability of the 3D density models (Kaban et al., 2022).

The Kalahari Craton represents an ideal study area to investigate the link between the nature and distribution of the thermo-compositional heterogeneities of the upper mantle and complex lithospheric tectonic evolution. Indeed, its cratonic lithosphere has been partially re-worked by various magmatic events, promoting a significant metasomatization (Griffin et al., 2003). In addition, the extensive collection and analysis of xenoliths in this area (e.g., Simon et al., 2003; Griffin et al., 2003; Faure, 2010; Tappe et al., 2018) provide tighter constraints on the compositions used in our approach, while also allowing us to verify the robustness of the obtained results.

2. Regional tectonic setting and crustal structure

The Kalahari Craton (Fig. 1a) comprises two Archean nuclei, the Kaapvaal and Zimbabwe cratons, surrounded by several Proterozoic mobile belts (e.g., Kachingwe et al., 2015). The Zimbabwe Craton includes the central Tokwe Gneiss Terrane (East Tokwe Block, 3.6–3.3 Ga), a younger accretionary terrane in the northwest (West Tokwe Block, 3.2–2.8 Ga), and late-stage greenstone belts (2.7–2.6 Ga) marking the craton's stabilization (Jelsma and Dirks, 2002). Its last major tectono-thermal event was the emplacement of the Great Dyke at ~2.58 Ga. The Kaapvaal Craton is a collage of Archean terranes mainly composed of granitoid–gneiss complexes and narrow greenstone belts that accreted and stabilized between 3.7 and 2.7 Ga (de Wit et al., 1992; Begg et al., 2009). It can be subdivided into: the Southeastern Terrane (Swaziland and Witwatersrand terranes, sutured at ~3.2 Ga) with NE–SW-trending gneisses and greenstone belts; the Central Terrane, a narrow block lacking greenstones; the Pietersburg Terrane, containing NE-trending belts; and the Western Terrane (~2.65 Ga), including the Kimberley Terrane, dominated by granites and gneisses with narrow N–S-trending belts (Fig. 1a). Between the Kaapvaal and Zimbabwe cratons is the Limpopo belt: an ancient microcontinent characterized by its own deformational style, which remained trapped between the two cratons, during their collision. The high metamorphic grade of the outcropping rocks of the Limpopo belt expresses crustal thickening, occurred during this collisional phase (Limpopo Orogeny, ~2.7 Ga), which lead to the currently unified Kalahari Craton.

During the collision, the Limpopo Terrane was thrust over the Zimbabwe Craton, while the Kaapvaal Craton was forced beneath it, resulting in the granulite-facies rocks seen in the Limpopo Belt today. The Kheis belt (~2.0 Ga), along the Western limit of the Kaapvaal craton, is commonly considered as its Mid-Proterozoic passive margin, deformed in Late Proterozoic time (e.g., Griffin et al., 2003), whereas the Namaqua-Natal belt, along the southern limit of the craton, is likely a Mesoproterozoic terrane accreted to the Kalahari Craton at about 1.2 Ga (e.g., Matthews, 1981) and the Magondi Mobile Belt, composed of a succession of metasediments, accreted to the northwestern part of the Zimbabwe craton in the Early Proterozoic (Fig. 1a).

The Kalahari Craton was affected by some tectono-thermal events, such as the Bushveld (2.05 Ga), which produced huge amounts of mafic and ultramafic intrusive rocks, covering an area of >60,000 km^2 in the Central and Pietersburg Terrane, and Ventersdrop (2.5–2.7 Ga) in the northwestern and central part of the Kaapvaal craton. It was also subjected to major flood-basalt events, such as the Karoo (183 Ma), due to the breakup of Gondwanaland in Jurassic time (e.g., Barton et al., 1994).

The crustal structure of the southern African cratonic areas, as detailed in Youssof et al. (2013), reveals a complex and heterogeneous composition shaped by various tectonic and magmatic processes over geological time. Their study identifies significant variations in crustal thickness and Vp/Vs ratios across the region. The Archean crust of the Kaapvaal and Zimbabwe Cratons generally exhibits thinner crustal profiles, with Moho depths ranging from 34 to 40 km, characterized by sharp, well-defined crust-mantle boundaries. In contrast, the tectonically reworked areas, such as the Limpopo Belt and the Bushveld Intrusive Complex, display thicker crust, ranging from 45 to 50 km, and more mafic compositions, indicative of extensive magmatic intrusions (Fig. 1b).

Youssof et al. (2013) also highlights the influence of ancient tectonic events on the crustal architecture. The central Kaapvaal Craton shows a relatively uniform crustal thickness with high Moho sharpness, while the Limpopo Belt, which experienced significant compressional events, reveals a more complex structure with varying thicknesses and compositions (Fig. 1b). Notably, the Bushveld Intrusive Complex stands out with its massive mafic intrusions and deep crustal roots, which have influenced the regional crustal evolution. These findings underscore the intricate interplay between tectonic, magmatic, and sedimentary processes in shaping the cratonic crustal structure of southern Africa regions.

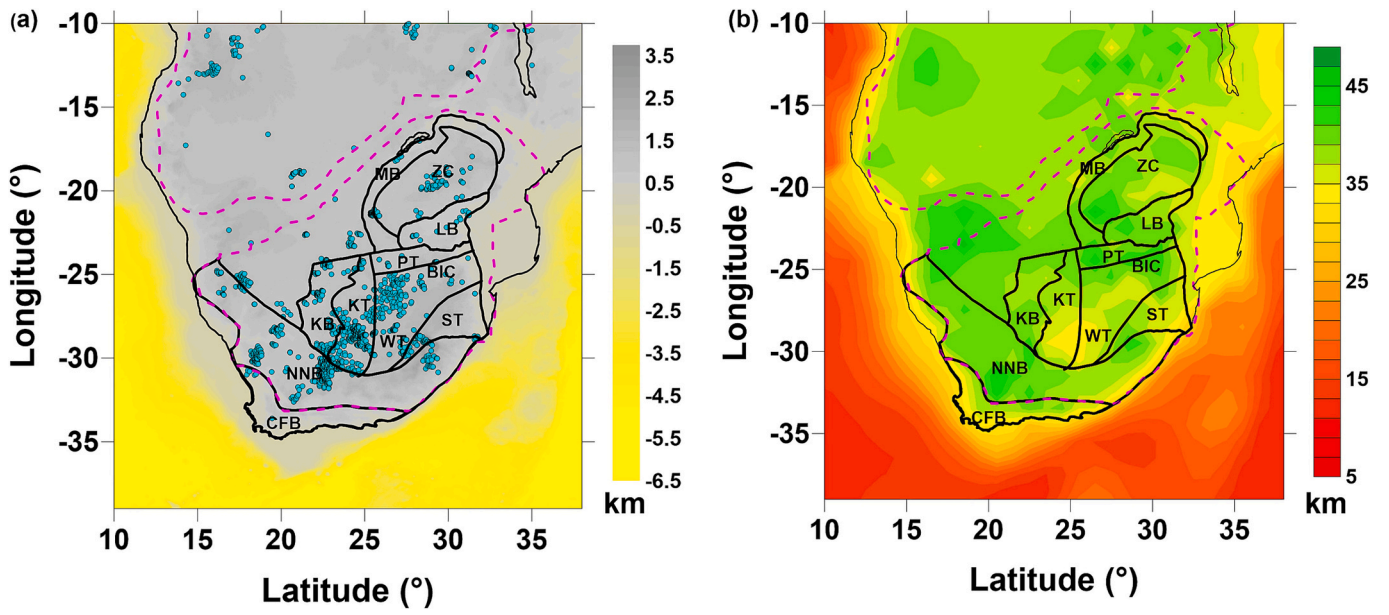

Fig. 1. (a-b) Surace topography map (Becker et al., 2009) (a) and Moho depth (Youssof et al., 2013) of the Kalahari craton (b). Cyan circles displayed in (a) show the kimberlites location (Tappe et al., 2018). Black and dashed magenta contours show the main tectonic features and the limits of the Mesoproterozoic terranes, respectively. Abbreviations stand for: BIC: Bushveld Intrusive Complex, CFB: Cape Fold Belt, KB: Kheis Belt, KT: Kimberley Terrane; LB: Limpopo Belt, MB: Magondi Belt, NNB: Namaqua-Natal Belt; PT: Pietersburg Terrane; ST: Swaziland Terrane; WT: Witwatersrand; ZC: Zimbabwe Craton.

3. Upper mantle heterogeneity of the Kalahari craton

The xenolith record from the Kaapvaal Craton indicates that the mantle lithosphere was broadly chemically depleted, probably during craton formation in the Archean, due to the large extraction of basalt and komatiite, and subsequently re-enriched by metasomatic fluids, due to major magmatic events, that may have gradually altered the mantle lithosphere and generated considerable changes in its composition (e.g., Griffin et al., 2003). Griffin et al. (2003) identified a group of kimberlites (named 'Group 1'), of age 105–70 Ma, prevalently located in the southwestern part of the Kaapvaal Craton, with a metasomatic signature, showing interaction of the lithosphere with mafic silicate melts, which resulted in garnets with high Zr, Ti, and Fe (Kobussen et al., 2009). On the other hand, another group of kimberlites (named' Group 2′), of age 150–115 Ma, mostly present in the southeastern part of the Kaapvaal Craton, shows metasomatism consistent with the interaction of the host peridotite with a hydrous, highly alkaline fluid (phlogopite-style metasomatism), resulting in high Zr, but low Ti and moderate Fe and is associated to a cooler lithosphere, with respect to the first group. Furthermore, in 'Group 1′, the degree of melt-metasomatism increases rapidly at depths >160 km, producing a sharp drop of the mean forsterite (*Fo*) content of olivine below 150 km, suggesting that the depleted lithosphere does not extend below ca. 170–175 km, while in 'Group 2′ the *Fo* remains almost constant even at larger depth (up to ~200 km). Furthermore, 'Group 2′ has a higher proportion of garnets from depleted harzburgites and lherzolites (Griffin et al., 2003). Therefore, the lithospheric mantle, sampled by 'Group 1′ kimberlites, has been interpreted as metasomatized and mixed with younger material during Paleoproterozoic to Mesoproterozoic rifting and compression, while that sampled by 'Group 2′ kimberlites, as more representative of the original Archean composition (Griffin et al., 2003). Besides these two groups of xenoliths, it was identified the Premier suite in the Central and Pietersburg Terrane of the Kaapvaal Craton, particularly rich in *Fe*, which erupted ~800 Ma after the intrusion of the Bushveld Igneous Complex and has a composition connected to the intraplate magmatic event (Griffin et al., 2003; Hoal, 2003). On the other hand, the Zimbabwe Craton has a very limited xenolith coverage and the only clues concerning its compositional heterogeneity have been derived from geophysical data (e.g., Afonso et al., 2022).

Seismological studies (e.g., James et al., 2003; Fouch et al., 2004; Youssof et al., 2015; Celli et al., 2020) have shown that the present-day thick, seismically fast mantle keel extends to deeper level than the depth of the xenolith samples, but laterally it does not extend below the entire surface expression of the cratonic region. Indeed, there are areas of relatively low *Vp* within the craton, which largely correspond to those affected by the progressive refertilization of the Archean root during episodes of intraplate magmatism, including the Bushveld Complex (2 Ga) and Karroo (ca. 180 Ma) magmatic events (e.g., James et al., 2003; Griffin et al., 2003; Celli et al., 2020). On the other hand, areas of high *Vp* are those having a relatively less metasomatized Archean upper mantle. The relatively low *Vp* of the upper mantle beneath the mobile belts around the craton is consistent with a more fertile composition (e.g., Griffin et al., 2003). The compositional variation of the southern African cratonic lithosphere has been also observed from receiver function analyses (Sodoudi et al., 2013), which revealed an irregularly stratified lithospheric structure of the Kalahari craton, related to frozen-in anisotropy and significant compositional changes.

4. Data input

4.1. Seismic tomography model

In order to perform the inversion of the seismic velocities into temperature on a global scale, we embed the regional seismic tomography model of Youssof et al. (2015), derived from a teleseismic tomographic inversion of the S-body wave dataset recorded by the Southern African Seismic Experiment (SASE), into the continental tomographic model of Celli et al. (2020), which is constrained by global dataset of waveform fits of over 1.2 million vertical-component, broadband seismograms. This continental model is integrated into the global upper-mantle, vertically polarized shear wave velocity model developed by Schaeffer and Lebedev (2013). In order to smooth the transitions occurring at the boundaries of the models, we leave a buffer zone of 100 km wide, in which the velocity anomalies of the datasets are interpolated using the kriging method (SURFER Golden Software, https://www.goldensoftware.com). Indeed, although the focus of this study is regional, the

calculations have to be necessarily performed on a global scale. This approach is required because the subsequent inversion procedure of the residual gravity and topography fields is carried out in the spherical harmonic domain (see section 5). If the inversion would be limited to a regional window, long-wavelength contributions from outside the study area would not be properly accounted for, potentially biasing the results.

The choice of the regional model of Youssof et al. (2015) embedded into continental (Celli et al., 2020) and global (Schaeffer and Lebedev, 2013) models is motivated by its unique resolution advantage. Indeed, it incorporates regularization through spatial smoothing and damping consistent with finite-frequency body-wave inversions, which limits the recovery of features smaller than the nominal resolution, while ensuring model stability and robustness. Embedding the regional model allows us to preserve fine-scale features, where the resolution is the highest, while still maintaining global consistency at the boundaries of the model domain. This strategy provides more reliable constraints for temperature inversion and compositional modeling than would be possible with global models alone. Unlike global models, which tend to smooth lateral variations, the Youssof et al. (2015) dataset, using the dense SASE stations coverage, resolves small-scale lithospheric structures, such as the Colesberg Magnetic Lineament (CML), a lithospheric-scale suture zone between the eastern and western blocks of the Kaapvaal Craton and the complex mantle structure beneath the Bushveld Complex (Youssof et al., 2015).

The analysis using finite-frequency P- and S-body wave tomography demonstrated that the fast lithospheric keels extend to depths of 300–350 km beneath the Kaapvaal Craton and 200–250 km beneath the southern Zimbabwe Craton (Youssof et al., 2015). The shear wave velocities variations at a depth of 100 km (Fig. 2a) show that the highest values are located in the western part of the Kaapvaal and Zimbabwe cratons (Kimberley Terrane and Western Tokwe Block). Looking at the two cross-sections (Figs. 2c-d), we observe a general progressive increase of velocities through depths, in particular in the Zimbabwe Craton. We can also notice a sharp lateral variation from the low to the high velocities, in the southwestern part of the study region, at the transition between the Namaqua belt and Western Terranes. On the other hand, in the southeastern region, a similar transition is located within the Kaapval Craton, at the most peripheral part of the Southeastern Terrane, at a depth of 100 km, and shifted more to the NE at larger depths (Fig. 2a-b).

4.2. Initial gravity field

The initial free-air disturbances are taken from the EIGEN-6c4 model (Förste et al., 2014). It is important to note that this model, up to a resolution of about 70 km, is based exclusively on satellite data, and therefore does not depend on terrestrial observations. The vertical gravity gradient (g_z) of GOCE is taken at the altitude of 225 km (Boumann et al., 2016).

5. Method

We first calculate and subtract the gravitational effects of the crustal layers from the observed gravity field, vertical gravity gradients, and surface topography (taken from Becker et al., 2009). This step isolates the residual fields that reflect mantle density anomalies (Fig. 3). Temperature variations in the uppermost mantle are then estimated from seismic tomography, assuming an initially uniform composition (named C1, see section 5.2), representing a re-fertilized condition of the South African cratons. Calculations were performed using PERPLE_X (Connolly, 2005), anelasticity effects are included (see Section 5.2). We then remove the density variations caused by temperature in the upper mantle from the residual gravity, gravity gradients, and topography. To avoid bias from deep sources, the effects of deep density anomalies below the maximum modeled depth (325 km) are also removed, using the global dynamic model of Kaban et al. (2015). Although this effect is

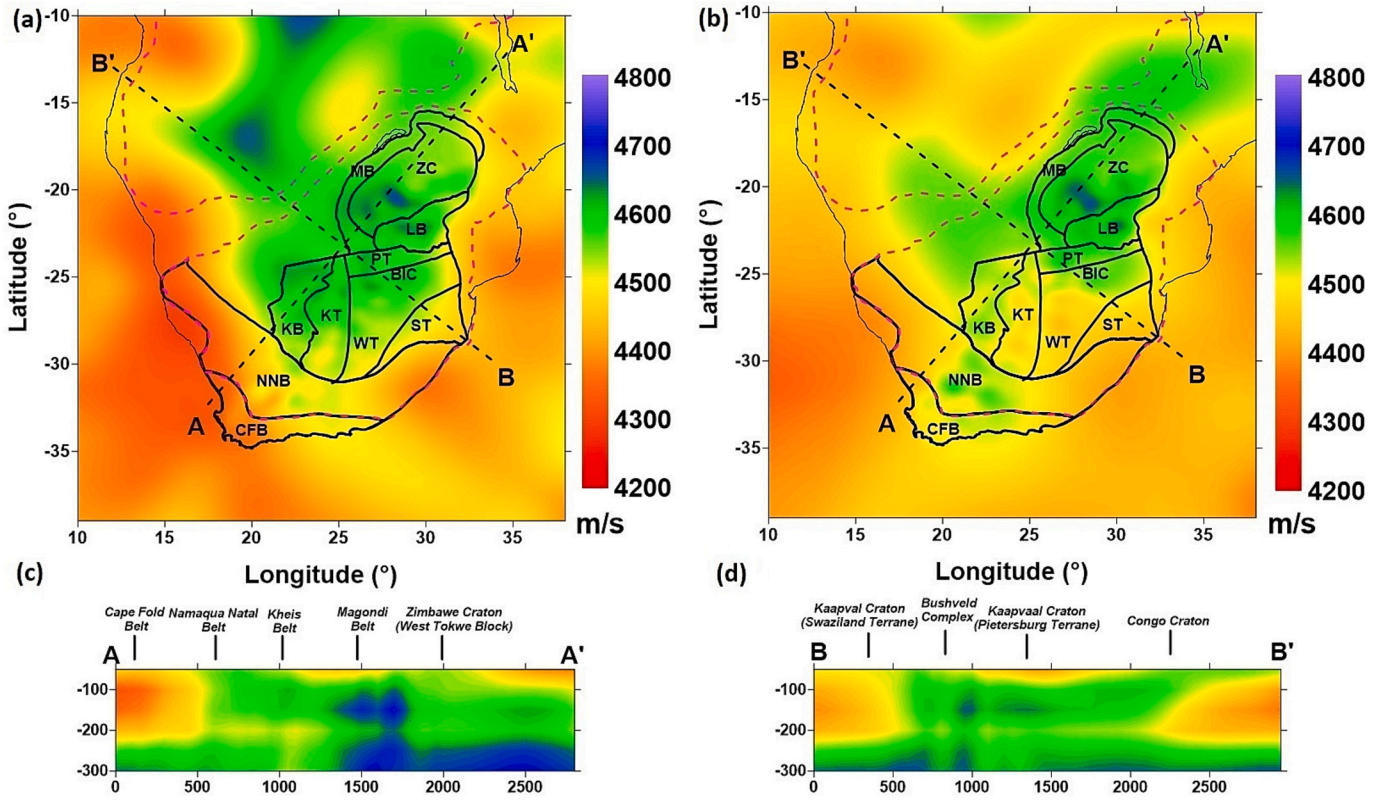

Fig. 2. (a-b) Seismic velocity variations at a depth of 100 km (a) and 200 km (b), respectively, and along two cross-sections (c-d), whose location is shown as dashed black lines (in a-b). Other features are as in Fig. 1.

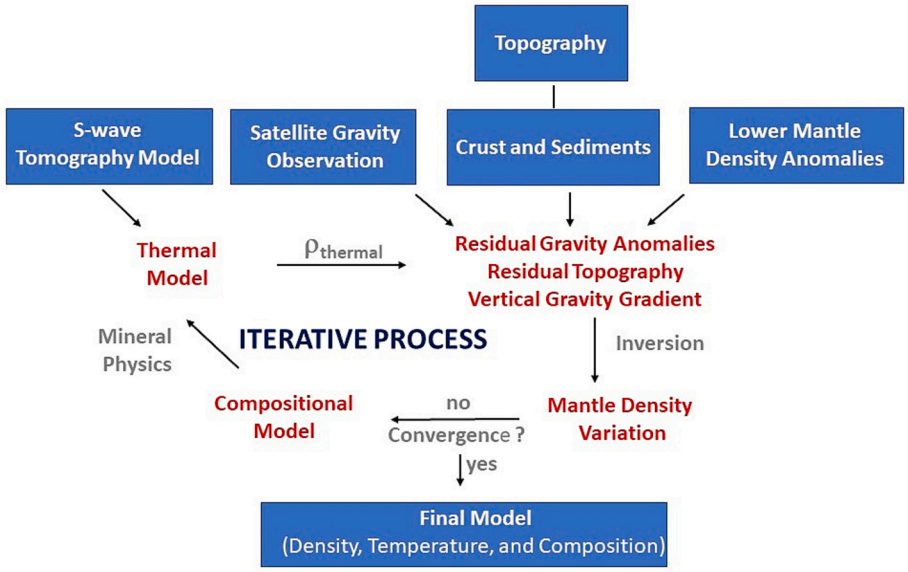

Fig. 3. Workflow showing the main steps of the iterative technique applied in this study to calculate the temperature, considering the compositional variations. To enable this iterative process, seismic velocities are first converted into temperature using a uniform composition. Residual mantle gravity and residual topography are calculated by removing the crustal effect from the observed gravity field. After correction for effects of the thermal model, these fields are jointly inverted (first inversion) to identify further density variations, which are interpreted to be of compositional origin. The same fields are also jointly inverted with the vertical gravity gradient (second inversion). Afterwards, the initial thermal model is updated, according to the results obtained by both inversions, giving the staring to the next iteration. The convergence is reached when density changes after the next iteration are within 1% variation limit (see main text for further explanations).

negligible at regional scale, its removal is necessary in the global inversion framework. The resulting residual fields are then inverted to obtain a 3D density model of the upper mantle, which complements the initial temperature-induced variations and forms the basis for estimating compositional changes.

We construct two alternative models: the first one is based on the residual gravity and topography as reported in previous studies (e.g., Kaban et al., 2014a, 2014b; Tesauro et al., 2014), while the second model is performed using the residual vertical gravity gradients from GOCE as an additional constraint (Kaban et al., 2022). The obtained compositional variations are employed to correct the temperature estimations to be used again in the inversion. These steps are repeated, in order to refine iteratively both the upper mantle temperature and composition, until the convergence is reached (Fig. 3). We assume that this occur when the density changes after the next iteration are within 1% variation limit. Below we describe in more details the main steps of the applied method.

5.1. Residual mantle anomalies

To compute the residual (crust-free) fields, we use the crustal model of Finger et al. (2022), which provides thickness and density of the main crustal layers, based on almost all available data (Global Seismic Catalog of Mooney, 2015 with updates up to 2019). The crustal gravity effects are calculated relative to a 1D reference model (Table 1). While the reference model only influences the absolute level of all fields—a factor typically disregarded in such studies (e.g., Mooney and Kaban, 2010)—we adopt the same model as in previous studies (e.g., Kaban et al., 2014a, 2014b; Tesauro et al., 2020). This approach enables a direct comparison of the anomaly amplitudes.

In the calculation of topographic and bathymetric gravity effects, densities of 2.67 g/cm^3 for continental rocks and 1.03 g/cm^3 for water are assumed (Table 1). The crustal effects have been estimated by a 3D method with all spherical effects included, as described in Kaban et al. (2016b). Comparison with other methods demonstrates that its accuracy regarding the gravity field is within a few mGal, which is more than adequate for studies of this nature (Root et al., 2016).

Table 1
Reference density model.

	Upper crustal layer	Lower crustal layer	Subcrustal layer
Depth (km)	0–15	15–40	40–75
Density (g/cm^3)	2.7	2.94	3.32

We compute the residual mantle gravity anomalies, vertical gravity gradients and residual topography, by removing the effects of the crust from the observed fields (Figs. 4a-c). In addition, we also remove the effect of the deep mantle below the bottom of the model. This is done based on global dynamic models as described in (Kaban et al., 2015). As observed in previous studies (e.g., Kaban et al., 2014a, 2014b; Tesauro et al., 2020; Finger et al., 2021; Finger et al., 2022; Kaban et al., 2022), the mantle gravity anomalies and vertical gravity gradient are inversely correlated with the residual topography and their amplitudes vary in a similar way after an appropriate scaling (Fig. 4b-c). Focusing on our study area, the Southeastern Terrane, the northern part of the Zimbabwe Craton (Tokwe block), and the northwestern part of the Namaqua-Natal Belt are characterized by significant negative mantle gravity anomalies (~200 mGal) and positive residual topography (~4 km), indicating that they are under compensated. In contrast, the Western Terrane shows strong positive mantle anomalies (> 200 mGal) and negative residual topography (about −1 km), which reflect over compensated conditions (Fig. 4a-b).

5.2. Initial thermal and density model of the upper mantle

We determine the thermal and corresponding density structure of the upper mantle by inverting seismic velocities. The thermodynamic modeling is performed with Perple_X (Connolly, 2005), which generates synthetic S–wave velocities and densities, corresponding to the physical conditions of the uppermost mantle. In Perple_X, physical properties are computed for a given mineralogical model as a function of pressure (P) and temperature (T). It performs a Gibbs free energy minimization to determine the mineral phase relations at each (P, T) point in the model and computes the bulk elastic properties of the mineral assemblage via an equation of state (Connolly, 2005). We used the thermodynamic

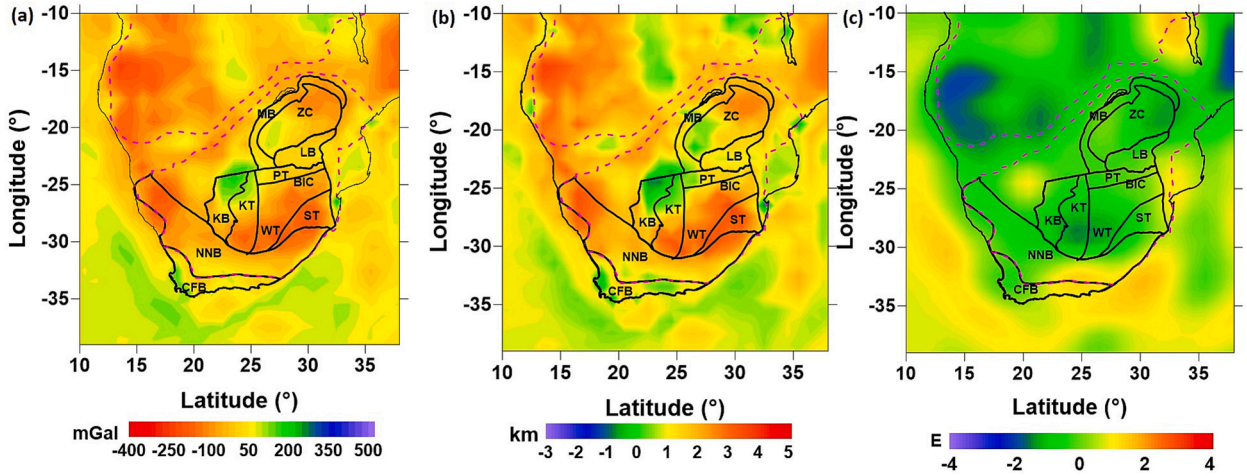

Fig. 4. (a-c) Mantle gravity anomalies (a), Residual topography (b), Vertical gravity gradient (g_z) of GOCE (c). Other features are as in Fig. 1.

database of Stixrude and Lithgow-Bertelloni (2022) based on Mie–-Gruneisen formulation, which is the most comprehensive database of upper mantle phase relations and seismic-wave speed calculations. In this way, we obtain the synthetic shear wave velocity, due to the anharmonic effect in the chosen range of pressure (0–10 GPa) and temperature (0° to 1800 °C).

The composition is chosen assuming two end-members chemical bulk compositions (C1 and C6, Table 2) in the NCFMAS system (Na2O-CaO-FeO-MgO-Al2O3-SiO2), which could be representative of a refertilized and refractory cratonic lithosphere of the southern African regions, respectively. To this purpose, we refer to the xenolith composition BD2452 of Griffin et al. (2004) and LET8 of Simon et al. (2003). The sample BD2452 was collected from the Kimberley area (Western Terrane) and is characterized by CaO, Al_2O_3 and FeO enrichment, implying modification by metasomatic processes (Griffin et al., 2004). Its composition differs from that representing a primitive mantle (e.g., McDonough and Sun, 1995), having in comparison a lower and higher amount of Al_2O_3 and MgO, respectively. The LET 8 sample derives from the Letseng-la-Terai, Matsoku pipe and represents a spinel peridotite or highly depleted harzburgite that does not contain garnet, because of their highly refractory character, but equilibrated in the garnet stability field (Simon et al., 2003). This sample belongs to the Lesotho xenolith suite, located in northern Lesotho on the southeastern margin of the Kaapvaal Craton and derived from 60 to 150 km depth. This suite has an elevated modal olivine content (between 53% and 76%) and Mg# in olivine (from 91.8 to 93.7). It is characterized by a strong depletion in FeO, CaO, and Al_2O_3 and its formation has been interpreted as residue from large volume melting in the Archaean. The two samples, among those belonging to the two xenolith suites, were chosen as reference compositions, since they show the largest difference in the amount of FeO and MgO. These oxides, being the most abundant (without considering SiO_2), produce the largest difference in density. After rounding the amount of iron of the two xenoliths from 8.93% (BD2452) and 5.89% (LET8) to 9% and 6%, respectively, we linearly interpolate the original percentage of the other oxides for the two new iron amounts. We obtain other intermediate reference compositions (C2-C5), with respect to the two end-members, by interpolating the defined percentages of the oxides, considering an amount of iron of 8.5%, 8.0%, 7.5%, 7.0%, and 6.5%, respectively (Table 2). In this way, we could simulate the different degree of metasomatism affecting the lithosphere of the Kaapvaal craton. Although we are aware that the melting trends of a natural peridotite sample can be non-linear, we make this assumption, in order to obtain a linear density variation between the two end-member density values. In this way, we could estimate the average difference in density between two close reference compositions (~0.008 g/cm^3), which defines the minimum amount of depletion that can be compensated by varying the composition from the first (C1) towards the second (C6) end-member (Table 2). This proceeding is needed to fit the negative residual densities, obtained from the joint inversion of the gravity fields with the density corresponding to a composition more depleted in heavy constituents (C2-C6, Table2). In contrast, we associate the more fertile composition (C1, Table 2) to the areas characterized by positive or negative residual densities lower than the compensation threshold (<0.008 g/cm^3). The oxides variations between the two end-members compositions produce a difference in the average percentage of the main mineral phases (Table 3). In particular, the amount of the olivine and OPX is relatively high in both end-members compositions (larger than 65% and 27%, respectively) and vary of about 7% and 3%, respectively. In contrast, the amount of the CPX and garnet is very small in both compositions (< 4%), but their relative variation is significant (Table 3).

The anharmonic velocities calculated with Perple_X for the different reference compositions, are corrected for the effect of anelasticity, which is evaluated through a quality factor *Q*. The latter is the inverse of the fraction loss of energy per wave cycle and is sensitive to several factors, such as the frequency of the seismic waves, temperature, and grain size in the upper mantle (Karato, 1993; Faul and Jackson, 2005), hydrous conditions, and presence of melt (Karato and Jung, 1998). In this study, we apply the anelastic models implemented by Cobden et al. (2018), which estimates the *Q* as dependent on pressure, temperature,

Table 2
Percentages of the oxides used in Perple_X to estimate the synthetic anharmonic velocities for the different reference compositions.

Oxides	C1	C2	C3	C4	C5	C6
SiO2	45.54	45.66	45.77	46	46.12	46.24
Al2O3	1.03	0.96	0.89	0.74	0.67	0.6
FEO	9	8.5	8	7	6.5	6
MgO	42.51	43.22	43.93	45.35	46.06	46.78
CaO	0.89	0.77	0.66	0.43	0.32	0.2
Na2O	0.07	0.07	0.06	0.05	0.05	0.04

Table 3
Average percentages of the main mineral phases formed using as input the percentages of the oxides representing the two end-member compositions, the re-fertilized (C1) and refractory (C6) one, respectively (Table 2).

Mineral Phases	C1	C6
Olivine	65.5	69.5
OPX	27.5	28
CPX	3.5	1
Garnet	3.5	1.5

seismic frequency, water concentration, and grain size. Among the provided models, we considered the one reproducing average hydrous conditions of the upper mantle ('*damp*' mantle, as defined by Cobden et al., 2018), as the most suitable for the study region. Indeed, most of the Kaapvaal craton have been affected by metasomatism with fluids injection, as observed by the analyses of the xenoliths (e.g., Griffin et al., 2003). On the other hand, 'wet' conditions, significantly enhancing the effects of anelasticity, are more appropriate for a mantle, which has lost most of its lithospheric roots, due to strong hydration, such as that of the North China Craton. We first estimate the temperatures by inverting the velocity of the seismic tomography model for the first end-member composition, representing re-fertilized conditions (C1), Fig. 5a-b. Afterwards, the temperatures are recalculated by varying the composition in each point of the grid, according to the amount of the negative density residuals, resulting from the two inversions (section 4.4).

5.3. Inversion of the gravity field, gravity gradients and residual topography into density variations

Before the inversion, we remove the effects of thermally induced density variations in the uppermost mantle from the initial residual mantle anomalies. Consequently, we focus on identifying perturbations in the initial density models outlined in the previous section.

For the first model, we jointly invert the residual gravity field and residual topography to refine the initial temperature-induced model of the uppermost mantle. These resulting corrections are considered to determine depletion in heavy constituents, characterizing the lithosphere composition in cratonic areas. In this joint inversion process, we also consider that the initial crustal model may have been biased by errors. Therefore, we also estimate perturbations of the crustal density to accommodate for the potential errors. The inversion procedure aims to minimize least square differences with the initial fields (g_{res} and t_{res}), while keeping minimal differences with the initial model (ρ_{ini}) (Kaban et al., 2015):

$$min\left\{ \|A\rho - g_{res}\|^2 + k_1\|B\rho - t_{res}\|^2 + \alpha\|\rho - \rho_{ini}\|^2 \right\} \quad (1)$$

where A and B are the operators for the gravity effect and dynamic topography induced by the density ρ, k_1 is the scaling factor for the residual topography, and α is the damping factor. k_1 represents a "natural" conversion factor from topography to gravity $(2\pi G\rho_t)^2$, where G is the gravitational constant and ρ_t is the density of the surface masses accounting for the topography variations (Kaban et al., 2015). The damping factor in eq. (1) is $\alpha = (2\pi GhD_n)^2$, where D_n is the normalized damping, h - the thickness of the elementary cell used in the inversion. The damping factor is selected according to the amplitude of the inverted density anomalies (Kaban et al., 2015). At the early stage, increasing the damping factor quickly suppresses the influence of noise. However, further increases cause the amplitude of the inverted density model to become overly smoothed. The optimal value $D_n = 0.75$ is determined globally (Kaban et al., 2015). The dynamic topography is computed using a prescribed viscosity structure, as described in (Kaban et al., 2015). In the inversion, we consider only radial variations in viscosity, which are typical for the continental lithosphere. Lateral viscosity variations, including weak plate boundaries, have a negligible influence on dynamic topography beneath South Africa and mainly produce very long-wavelength signals that do not affect the modeled upper-mantle anomalies (Kaban et al., 2014a, 2014b).

Therefore, this is an Occam type inversion (Constable et al. (1987), which requires minimal deflections from the initial densities as a precondition to regularize the solution. The inversion is performed in a spherical harmonic domain and thus global coverage for all data sets are needed. For the velocity variations in the upper mantle outside South Africa, we employ the seismic tomography model of Celli et al. (2020), which is embedded in the global model of Schaeffer and Lebedev (2013). The maximal horizontal resolution reaches 180 degree/order (1°x1° in space domain) and the vertical resolution for the mantle is 50 km. We adjust densities in 7 layers with the central depth from 15 to 300 km. As pointed out before, the uppermost layer is introduced to allow compensation of possible errors in the crustal model, since the density of the crystalline crust is the most uncertain parameter of the initial model.

The joint inversion of the residual gravity anomalies and residual topography provides a possibility to divide the effects of near surface

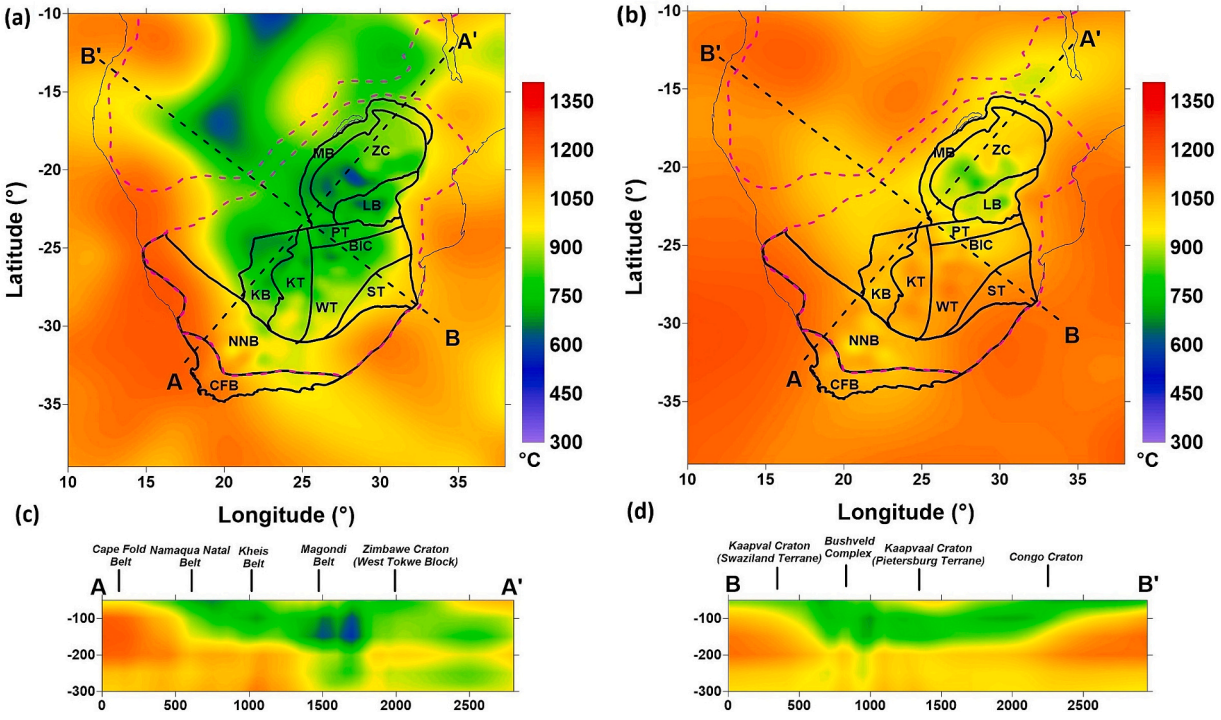

Fig. 5. (a-b) Initial thermal model of the upper mantle, using a uniform composition, at a depth of 100 and 200 km, respectively, (a-b) and along two cross-sections (c-d), shown as dashed black lines (in a-b). Other features are as in Fig. 1.

and deep density anomalies (Kaban et al., 2015). The 6 layers from 50 to 300 km (central depths) are related to the mantle structure. In the inversion, only density variations are determined relative to the global average value for each layer based on the Schaeffer and Lebedev (2013) tomography model converted to densities, as described in section 5.1. The standard deviation of the residual gravity field and the field of the inverted model (rms) is 6.7 mGal, while the standard deviation of the residual topography is 0.06 km. These values are nearly two orders of magnitude smaller than the amplitude of the anomalies, suggesting a strong fit between the model and the inverted fields. It has been shown that the relative pattern and sign of density anomalies in the upper mantle are effectively restored, but the amplitudes of these anomalies may be reduced a bit, due to damping of the final solution in the inversion. Therefore, they likely represent a lower limit of the actual density variations. More details of the method and discussion of potential uncertainties can be found in Kaban et al. (2015) and Kaban et al. (2016a).

The second model has been produced including the vertical gravity gradient, as additional constraint (Kaban et al., 2022). As before, the objective function is designed to minimize, in a least-squares sense, the differences between the final model and observed data across all three fields: residual gravity, vertical gravity gradient, and residual topography, with the gravity gradient extended from Kaban et al. (2015):

$$min\left\{\|A\rho_i - g_{res}\|^2 + k_1\|B\rho_i - t_{res}\|^2 + k_2\|C\rho_i - g_{z-res}\|^2 + \alpha\|\rho_i - \rho_{ini}\|^2\right\}, \quad (2)$$

where C is the integral operator converting density variations into vertical gradients, k_2 is the scaling factor for the gradients with respect to the gravity field, which is determined based on the relationship between standard deviations of these fields, and other parameters set as in Eq. 1.

6. Results

6.1. Initial temperature variations in the upper mantle

The conversion of velocity into temperature allows to identify the distribution of the cold and hot region in the study area and thus the lithospheric thickness variations in much higher details than just looking at the absolute velocities (Fig. 2a-b). The temperatures within the Kalahari cratons, at a depth of 100 km, mostly range between 500 °C and 900 °C, with the lowest values corresponding to the western Towke block and western part of the Kimberley terranes, while the hottest regions correspond to the southeastern border of the cratons. At a depth of 200 km, the temperature ranges from 800 °C to values above 1100 °C, indicating the vicinity of the asthenosphere. The lowest temperatures are mostly localized in the southern part of the Zimbabwe Craton (Fig. 5a-b). Looking at A-A' velocity cross-section (Fig. 2c), we observe a progressive thickening of the high velocity layer, which identifies the cold lithosphere (Fig. 5c), from the southernmost part of the study area (Cape fold belt) towards the northern part of the Kaapval craton (Kimperley Terrane). Farther to the north, the thickness of the high velocity layer remains almost unchanged (Fig. 2c and 5c). On the other hand, along cross-section B-B′, the thickening of the cold lithosphere occurs from the southeastern border of the Kaapvaal craton to the Western Terrane, while farther to the north, outside form the Kalahari cratons, the high velocity layer tends to be thin again (Fig. 2d and 5d). We can further notice a local lithospheric thinning in correspondence of the Bushveld Complex (Fig. 5a-b), possibly due to the tectonic event that metasomatized its mantle.

6.2. Final thermal, density, and compositional model of the upper mantle

The temperatures distribution at a depth of 100 km and 200 km, resulting from the two inversion types are very similar, showing values larger of about 100–150 °C, with respect to the initial thermal field (Figs. 6a-d and 7a-d). Indeed, the differences in the density variations, obtained from the two inversions, and, thus, in the amount of depletion,

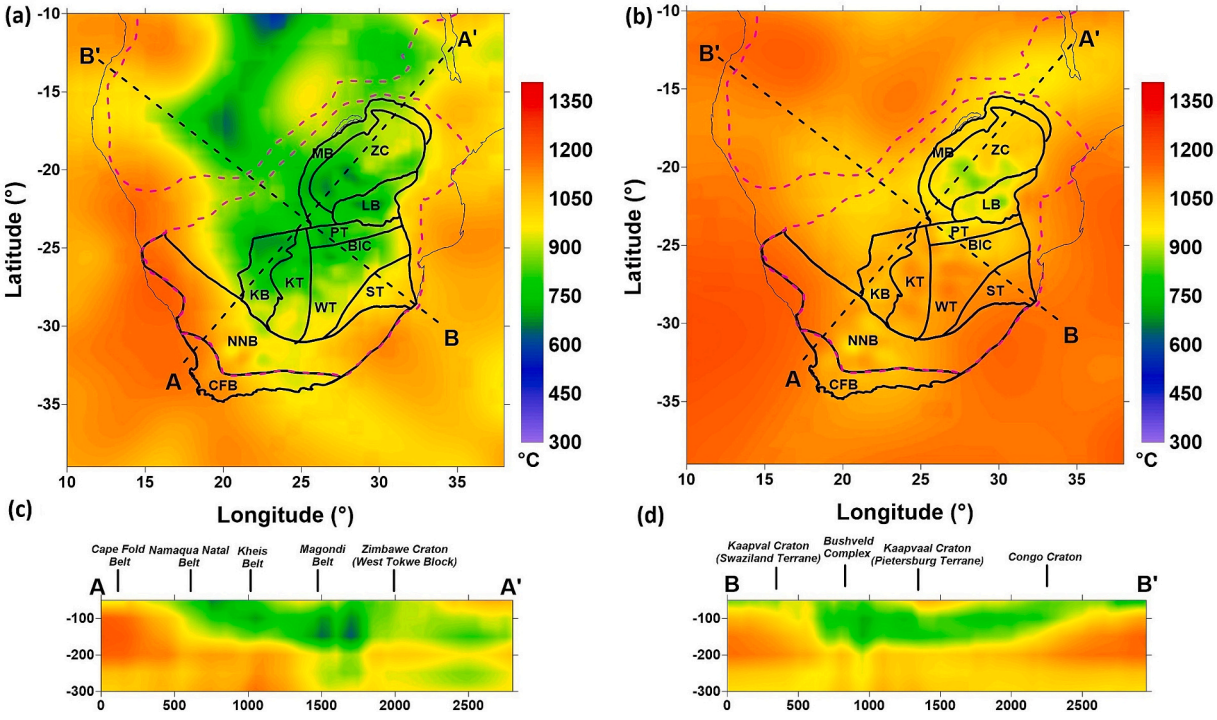

Fig. 6. (a-d) Final thermal model of the upper mantle obtained from the first inversion, at a depth of 100 and 200 km, respectively, (a-b) and along two cross-sections (c-d), shown as dashed black lines (in a-b). Other features are as in Fig. 1.

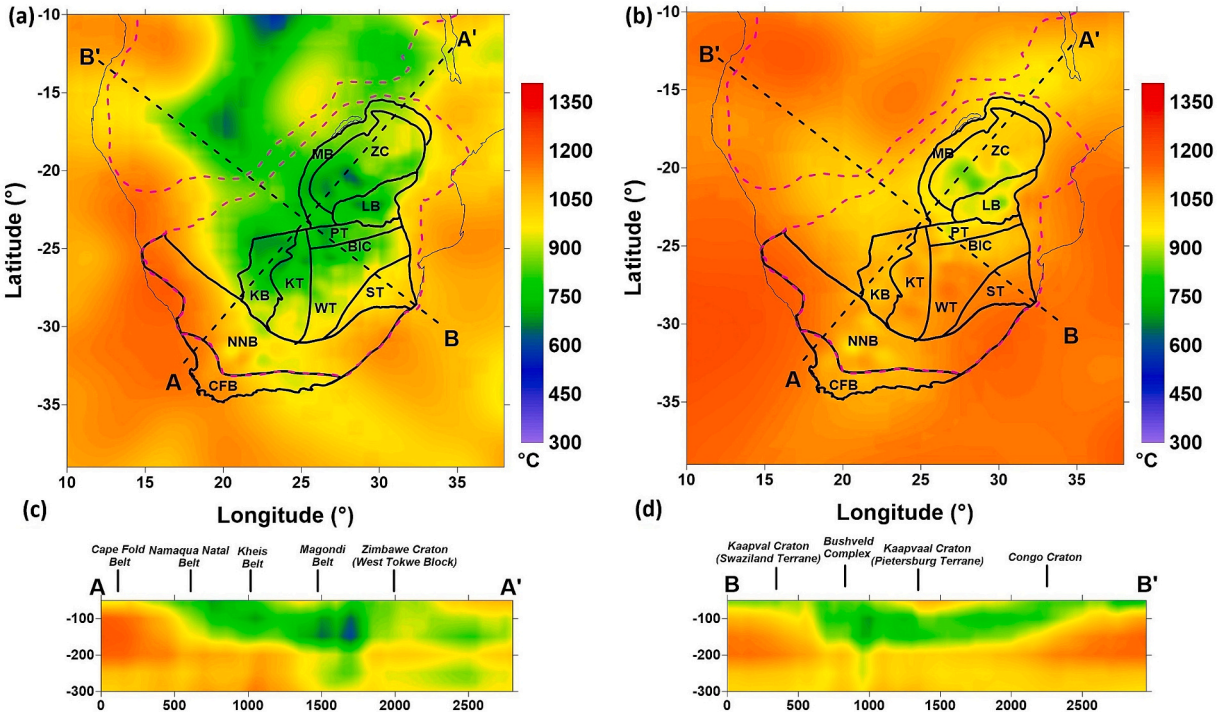

Fig. 7. (a-d) Final thermal model of the upper mantle obtained from the second inversion, at a depth of 100 and 200 km, respectively, (a-b) and along two cross-sections (c-d), shown as dashed black lines (in a-b). Other features are as in Fig. 1.

are quite small and do not produce significant temperature variations. The increase of temperatures, with respect to the initial thermal model, is observed in the areas of higher iron depletion (e.g., the Southeastern Terrane), at a depth of 100 km, while it is significantly reduced at larger depths (Figs. 6a-d and 7a-d).

Since the most significant depletion, as evidenced by the xenoliths' composition (e.g., Griffin et al., 2003; Simon et al., 2003) affects the shallowest mantle, we display the density and compositional changes at

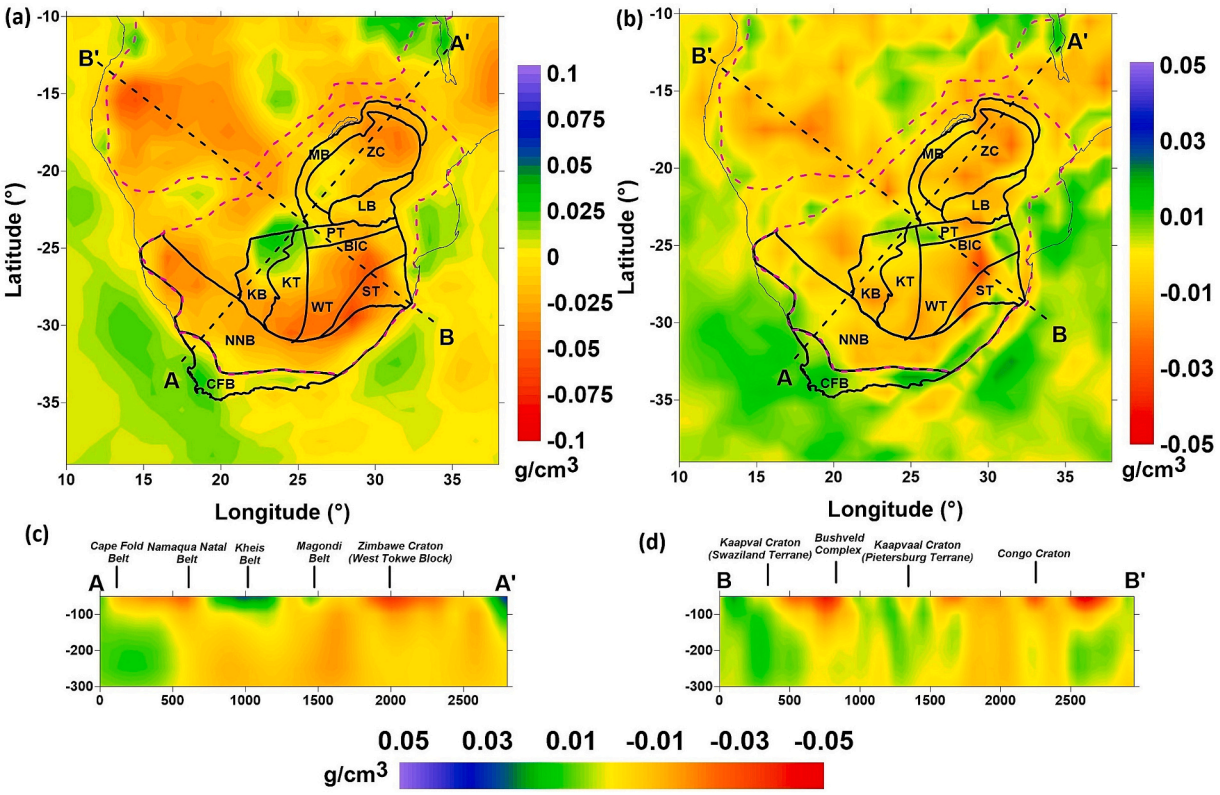

Fig. 8. (a-d) Final density model of the upper mantle, obtained from the first inversion, at a depth of 50 and 100 km, respectively, (a-b) and along two cross-sections (c-d), shown as dashed black lines (in a-b). Other features are as in Fig. 1.

a depth of 50 km and 100 km, as well as along the same two cross-sections used to display velocity and temperature variations (Figs. 2c-d and Figs. 5c-d). The final residual density distribution, obtained from the first inversion, spans within a range of ±0.1%, at a depth of 50 km, which is reduced almost to the half at a depth of 100 km (Figs. 8a-b). In addition, in the very shallow upper mantle, the negative densities form a broad anomaly over the Southeastern Terrane and northern part of the Zimbabwe Craton (Tokwe Block), while at a depth of 100 km, these anomalies persist, although reduced in size (Figs. 8a-b). On the other hand, the Western Terrane is undepleted or even characterized by weak positive residual density (Fig. 8a-b). The negative residual densities, resulting from the second inversion, show a similar distribution to those of the first inversion, although with a smaller amplitude at a depth of 50 km (Fig. 9a). In addition, the maximum depletion (about −0.03 g/cm^3) is localized on more limited areas. At a depth of 100 km, the density anomalies distribution become even more similar to those obtained from the first inversion, since the last ones have been reduced more significantly with depth (Figs. 8b and 9b). As we can observe from the cross-sections, the upper mantle becomes more homogeneous at larger depths, even if there is a persistence of the weak negative anomalies in some parts (<−0.01 g/cm^3, Figs. 8c-d and 9c-d). On the other hand, some lateral density contrast between the most depleted (Southeastern Terrane) and most refertilized areas (Western Terrane) extend also at large depths (Figs. 8c-d and 9c-d). These findings reflect the complexity and variability of the upper mantle structure in the Kalahari region, with implications for understanding its geodynamic evolution.

The compositional variations resulting from the fitting of the negative densities are represented in terms of change of the main mineral phases, such as olivine (the major constituent of the peridotite), OPX, CPX, garnet, as well as of *Fe* oxide (Figs. 8a-d, 9a-d, 10a-d, 11a-d and S1-S4). We can observe that the maximum range of variation in olivine is obtained for both types of inversion at a depth of 50 km and span up to 4% or 5%, depending on the mineral phase (Figs. 10a and 11a). Furthermore, the distribution of the percentages of olivine and CPX, as well as those of OPX and garnet are similar, but anticorrelated (complementary) in the amount (Figs. S1-S3). The increase of olivine and OPX percentage, characterizes the areas of larger depletion, being strongly correlated with the highest negative residual density anomalies and is accompanied by a decrease of the amount of CPX and garnet, respectively (Figs. 8a-d, 9a-d, 10a-b, 11a-b, S1-S3). We can notice that the olivine and OPX are present with significant percentage, also when the composition C6 is the input, while the percentage of CPX and garnet remains very small, reaching a maximum of less than 4% (Table 3, Figs. 10a-b, 11a-b, and S1-S3). In the following, we discuss the compositional variations only in terms of the lateral variability of the residual density anomalies coupled with those of the olivine percentage. The results of both inversions show that the areas with the highest negative density anomalies (between −0.075 and − 0.05 g/cm^3), compensated with the largest percentage of olivine, correspond to the northern part of the Zimbabwe craton (Tokwe Block) and eastern part of the Kaapvaal craton of Mesoarchean age (Swaziland, Witswatersrand, and Kimberley Terrane). On the other hand, the regions characterized by a significant refertilization of the upper mantle, where the negative density anomalies become negligible and olivine percentage drops below 67%, are mostly located in the western and northern part of the Kaapvaal craton, composing the Paleoproterozoic Terranes (Kheis belt, Kimberley Terrane, and Bushveld Complex), the western part of the Zimbabwe craton (Western Tokwe Block) and the terranes suturing the two Kalahari cratons (Limpopo Belt), both of Neoarchean age (Figs. 10a-b and 11a-b).

Looking at the cross-sections (Figs. 10c-d and 11a-d), we observe a sharp lateral variation in composition between the Mesoarchean terranes and the re-fertilized upper mantle characterizing the younger regions. Furthermore, we observe that at a depth below 150 km, there is a significant drop in the residual negative density anomalies and compensating olivine percentage (<0.01 g/cm^3 and < 67%,

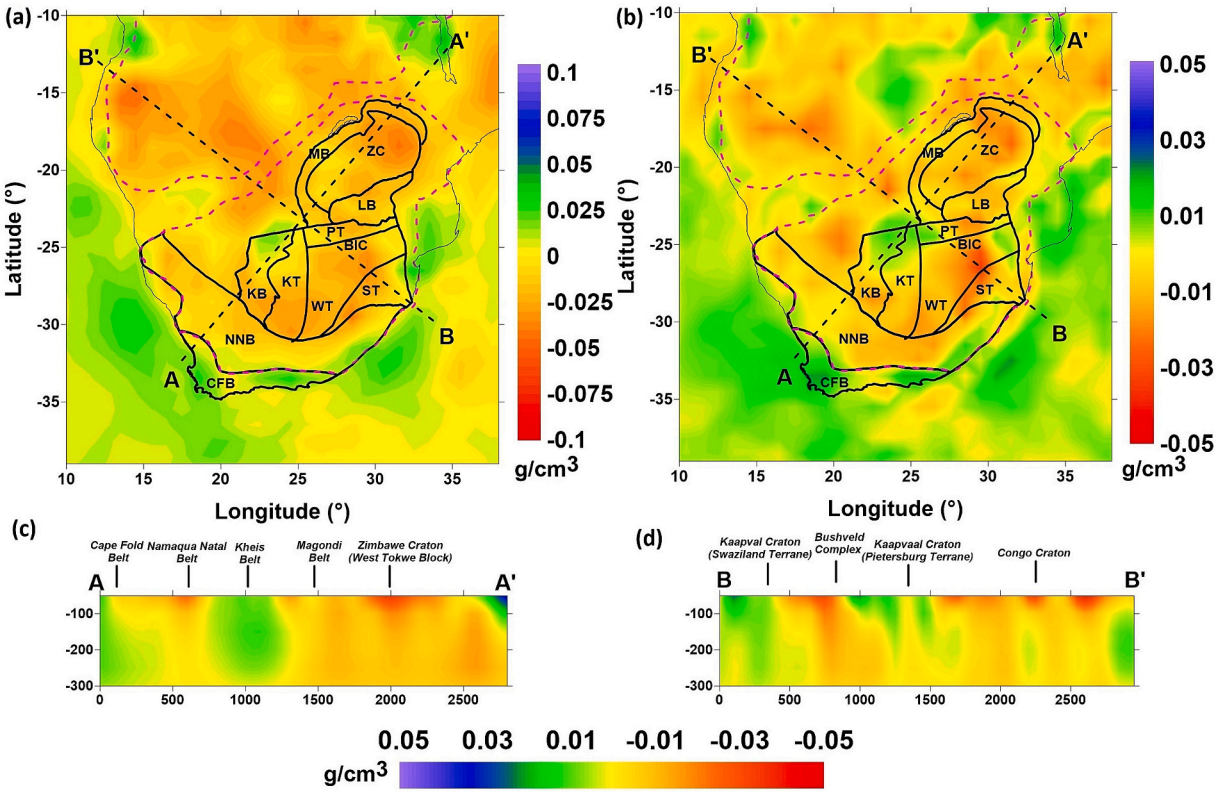

Fig. 9. (a-d) Final density model of the upper mantle, obtained from the second inversion, at a depth of 50 and 100 km, respectively, (a-b) and along two cross-sections (c-d), shown as dashed black lines (in a-b). Other features are as in Fig. 1.

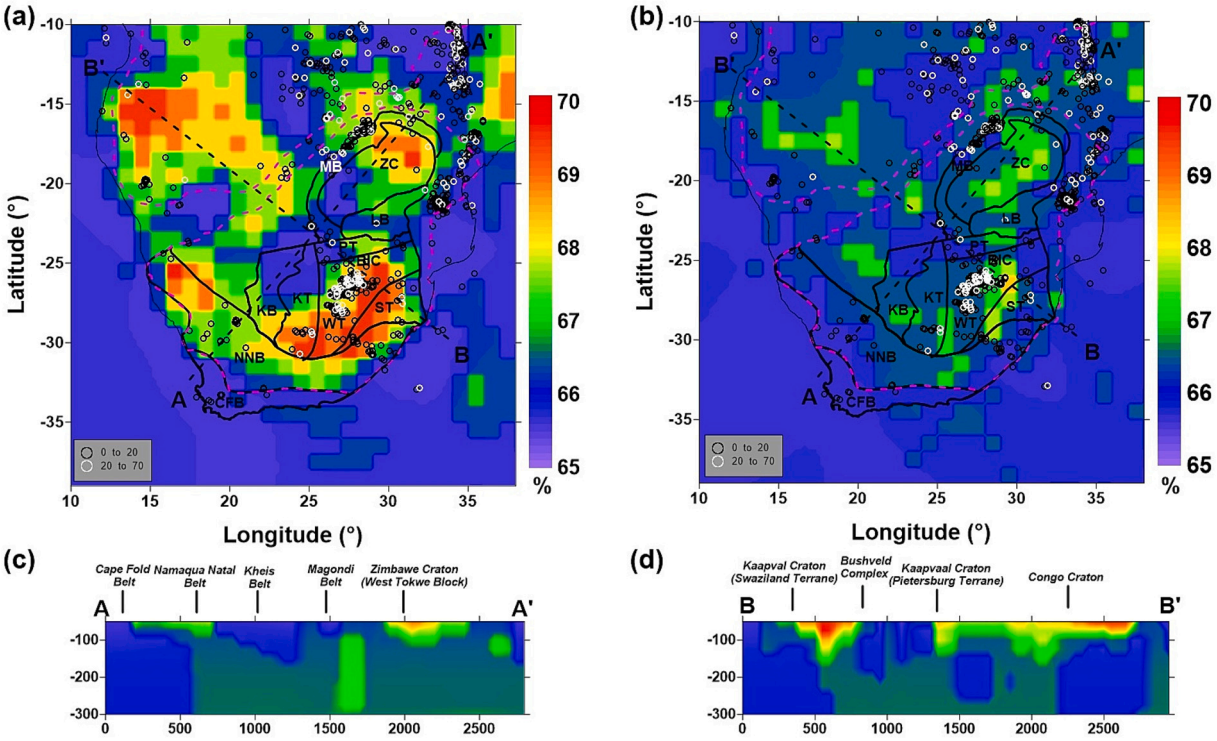

Fig. 10. (a-d) Compositional variation of the upper mantle in terms of olivine percentage, obtained from the first inversion at a depth of 50 and 100 km, respectively (a-b), and along two cross-sections (c-d), shown as dashed black lines (in a-b). Colored circles show the earthquakes location according to their depths. Other features are as in Fig. 1.

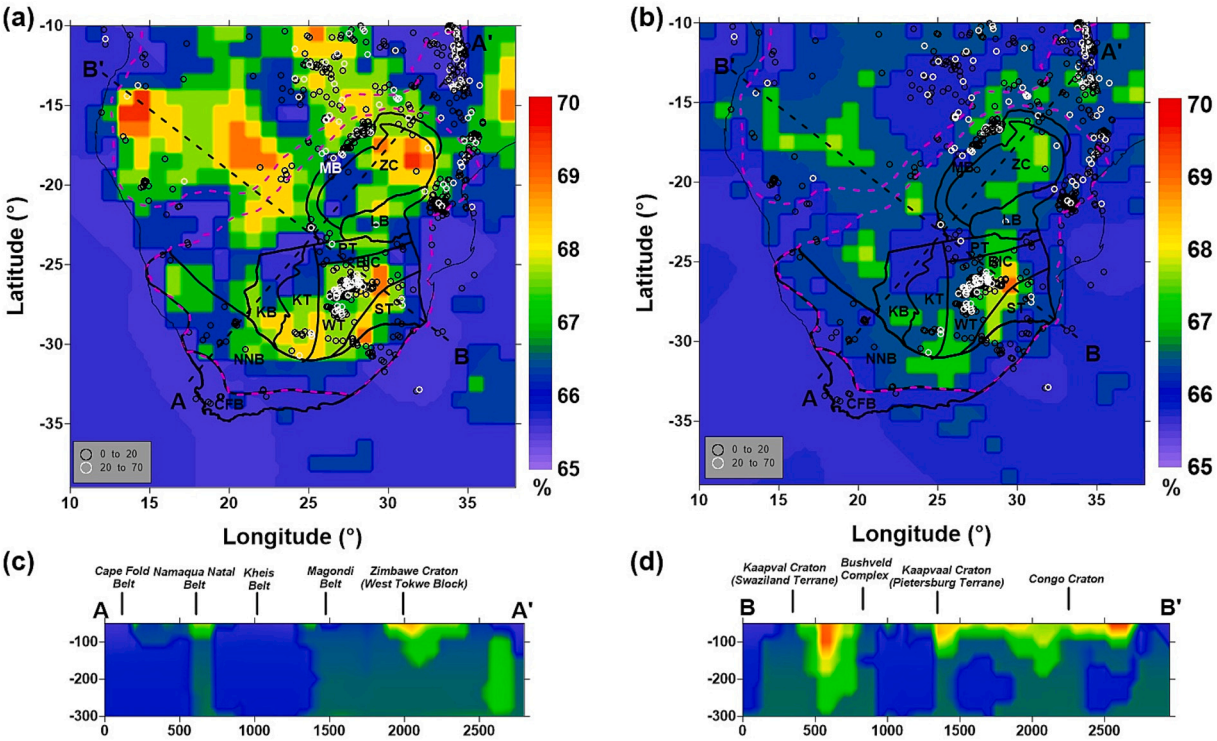

Fig. 11. (a-d) Compositional variation of the upper mantle in terms of olivine percentage, obtained from the second inversion at a depth of 50 and 100 km, respectively (a-b), and along two cross-sections (c-d), shown as dashed black lines (in a-b). Black and white circles show the earthquakes above and below the depth of 20 km, respectively. Other features are as in Fig. 1.

respectively). The only exception is the Mesoarchean Swaziland Terrane (part of the Southeastern Terrane), where moderate depletion (around -0.025 g/cm^3), resulting from the second inversion, is observed up to a depth of almost 300 km and the northern border of the Kaapvaal craton, where an increase of depletion is observed below 100 km depth (Figs. 9a-d and 11a-d). These results highlight the intricate relationship between compositional variations and thermal structure in the upper mantle, revealing key differences between ancient and younger tectonic features.

7. Discussion

Previous studies on the Kaapvaal Craton show a variable thickness of the cold lithospheric roots, spanning from 150 to 200 km (e.g., surface-wave studies of Priestley et al., 2006; receiver function from Sodoudi et al., 2006), to 250–300 km (e.g., body-wave studies of James et al., 2003), up to ~300 km (receiver function study by Wittlinger and Farra, 2007 and surface-wave studies by Sebai et al., 2006) or even beyond that depth limit as imaged by finite-frequency tomography (e.g., body waves seismic imaging supported by coherent quantitative sensitivity analysis by Youssof et al., 2015). Concerning the Zimbabwe craton, some studies predict cratonic roots thinner than those of Kaapvaal (e.g., receiver function from Sodoudi et al., 2006).

Looking at the seismic velocity distribution, at a depth of 100 km (Fig. 2a), we notice that the S-wavespeeds tend to increase northward, specifically from the Namaqua-Natal belt to the central part of the Kaapvaal and Zimbabwe craton, with a slight decrease beneath the Limpopo belt. At larger depths the fastest velocity is limited to the southern-central part of the Zimbabwe craton and a significant decrease is observed in the southern and eastern part of the Kaapvaal craton. On the other hand, we observe an increase of the S-wave velocities from east to west, in particular from the Southeastern to the Western Terrane. For this reason, the temperatures obtained from the inversion of the seismic data, assuming a uniform composition show a thickening (~200 km) of the cold layer (< 800 °C) beneath the Western Terrane of the Kaapvaal craton and the central-southern part of the Zimbabwe craton (Fig. 5a-b). These results are quite consistent with those of other seismic tomography models of the area, in particular, the low velocities that characterize the eastern terranes of the Kaapvaal craton are observed also in the dataset of Celli et al. (2020) and Schaeffer and Lebedev (2013). This feature can reflect the lithospheric thinning, as the effect of the thermal erosion that often act along the flanks of the cratons, due to micro-convection and/or plume uprising (e.g., Celli et al., 2020.). However, this area corresponds also to the part of the Kaapvaal craton more refractory, as observed from the results of both the first and second inversion (Figs. 10 a-d and 11 a-d). Such a correspondence can find an explanation in the type of re-fertilization that affected the upper mantle beneath the Kaapvaal craton, primarily involving silica enrichment, leading to the OPX formation. As before discussed, most of the xenoliths collected in the Kaapvaal craton, show a high silica content and thus a high percentage of the OPX. This type of metasomatism, due to fluids or melt infiltration can lower the seismic velocity (in particular, P-wave velocities), as demonstrated in the previous study of Boyce et al. (2021). However, the xenoliths belonging to Group 2, mostly located in the Southeastern Terrane, with respect to those belonging to Group 1, mainly located in the Western Terrane, have a significant higher MgO content, leading to the increase of olivine (and slightly of OPX) at the expenses of CPX and garnet, with a consequent density reduction.

The inclusion of the vertical gravity gradient in the second type of inversion leaves almost unaltered the lateral distribution of the iron depletion, but results in a decrease of its amount in the uppermost part of the mantle (at ~50 km) of the Kaapvaal craton (Fig. S4). Indeed, there, the maximum depletion is limited to the Swaziland Terrane. On the other hand, the results of the second inversion type show moderate depletion (Fe ~7%) extending at larger mantle depth (~250 km). The large difference in the results obtained from the two inversions at shallow mantle depths can be ascribed to the higher sensitivity of the gravity gradients to the near surface anomalies.

The previous study of Afonso et al. (2022) show a large uniform depleted lithospheric root underlain the Kaapvaal craton, up to a depth consistent with the bottom of the high-velocity lithosphere (about 175–200 km), but without significant lateral compositional variations, evidenced by our results and xenolith samples. The same authors observe another smaller region of depleted lithosphere, corresponding to the northern part of the Zimbabwe craton, consistent with our results. Therefore, as in our case, the results of Afonso et al. (2022) observe a more fertile upper mantle in the Limpopo belt and southern part of the Zimbabwe craton. These results are interpreted as signs of mantle modification through fertilization processes, potentially linked to collisional events that amalgamated the Zimbabwe and Kaapvaal cratons. The findings align with geochemical studies (Meibom et al., 2003; Anderson, 2006), suggesting that the collisional and magmatic processes significantly altered the lithospheric mantle, creating distinct compositional and structural heterogeneities. These areas were also partially affected by the Mesozoic Karoo magmatic event (183 Ma), likely in a same way as the formation of the Bushveld complex (2.05 Ga) and Ventersdorp (2.7 Ga) influenced the mantle lithosphere of the Kaapvaal craton. However, our results show within the two cratonic blocks lateral and in-depth variations of depletion, related to the different episodes of metasomatism that accompanied the plume activity and volcanism affecting them.

In particular, we observe that the significant refertilization of the cratonic upper mantle has reduced the original extent of the strongly depleted lithospheric mantle to mainly the Southeastern Terrane in the Kaapvaal craton up to the first 100 km of depth (Figs. 10a-d and 11a-d).

Looking at the earthquakes distribution (Figs. 10a-b and 11a-b), occurred from 1973 to the present-day with a magnitude between 2.5 and 7 (https://earthquake.usgs.gov/earthquakes/search/), we can observe that the shallowest ones (< 20 km) are partly located along the borders of the craton. Previous studies have already demonstrated a correlation between the location of these seismic events and the variation in the lithospheric thickness and rheology, usually characterizing the cratonic margins (e.g., Craig et al., 2011; Sloan et al., 2011; Mazzotti, 2007). In addition, there is a cluster of earthquakes occurring mostly in the deep crust/uppermost mantle, along the suture between the Western and Southeastern Terrane, marking the transition between crustal rocks of different age, as well as upper mantle with different density and composition (Figs. 8a-d, 9a-d, 10a-d, 11a-d). Therefore, we hypothesize that these lateral heterogeneities can influence the lithospheric stress distribution, favoring the earthquakes nucleation also below the shallow crust.

The most metasomatized part of the Kaapvaal craton corresponds to its edges (i.e. the Namaqua-Natal, Kheis, and Limpopo belt), since the upwelling mantle can reach shallower levels in the areas where the cold lithosphere has a reduced thickness and a higher-degree of decompression melting can form. On the other hand, a thicker and cooler cratonic root would favour the insulation of this part of the craton, promoting a reduced amount of alkaline melts, inducing metasomatism.

The accuracy of the thermo-compositional model for the upper mantle beneath the Precambrian shield of southern Africa is inherently linked to the uncertainties present in the underlying seismic velocity models, being the uncertainty of the density variations obtained from the inversions small (Tesauro et al., 2014). These include the quality and distribution of seismic stations, the density of ray coverage, and the assumptions made in the inversion process, such as the damping and smoothing parameters.

In particular, the resolution tests performed in previous studies, including finite-frequency and checkerboard tests, indicate that while horizontal resolution is relatively well-constrained (better than 100 km in the upper 200–300 km), vertical resolution is more susceptible to smearing effects, potentially extending over 100–200 km, decreasing with depth and reduced ray coverage. These vertical uncertainties can

influence the interpretation of lithospheric thickness and the depth extent of velocity anomalies. Consequently, any errors in the seismic velocity model are propagated into the thermal and compositional models, affecting the precision of temperature estimates and compositional variations. Other uncertainties are related to the choice of the anelastic model and of the two end-member compositions used to calculate the synthetic velocities. However, both of them should have only a minor effect on the estimated temperatures. Indeed, the anelasticity is temperature dependent and thus its effect is much more significant in the tectonically active regions than in the stable cratons. Considering the sensitivity of seismic velocities to temperature and composition, uncertainties in the inferred temperature structure are estimated to be on the order of several tens to about 100 °C in the upper lithosphere, corresponding to density uncertainties of a few 10^{-3} g/cm^3 (Tesauro et al., 2014). Concerning the choice of the reference end-members compositions, this was based on the xenolith samples representative of the different parts of the Kaapvaal craton, which produces a significant difference in terms of temperature and composition (up to ~200 °C, see section 5.2). However, the maximum depth of the xenolith samples is shallower (150–200 km) than the depth limit of our models (300 km) and thus the composition/thermal anomalies of the deep lithospheric mantle are not comparable with the petrological data.

Therefore, despite these challenges, the consistency of results across multiple seismic datasets and inversion techniques provides confidence in the general trends observed, though caution is warranted when interpreting finer-scale features.

8. Conclusions

This study provides a robust thermo-compositional model of the upper mantle beneath the Kalahari Craton, shedding new light on the intricate thermal and compositional variations within this ancient and stable region. By integration of the seismic tomography and gravity data, we have revealed various heterogeneities in the lithospheric structure, which are crucial for understanding the complex geodynamic history of the region.

The new models highlight significant lateral and vertical variations in mantle composition, particularly in areas associated with distinct refertilization (Western Terrane) and depletion signatures (Southeastern Terrane). The approach used have allowed us to contextualize subtle features within the broader mantle framework, demonstrating the model's effectiveness in capturing the intricate details of cratonic lithosphere dynamics. Indeed, although both the Kaapvaal and Zimbabwe cratons are still characterized by thick cold lithospheric mantle, we demonstrate that only some parts of the very shallow upper mantle (< 100 km) preserve the ancient depletion in heavy constituents.

While previous studies, such as Youssof et al. (2015), have identified relatively small lateral features like the Colesberg Magnetic Lineament (CML), our study provides a deeper understanding by integrating these results into a comprehensive thermo-compositional context. This not only strengthens the reliability of the model, but also emphasizes the effectiveness of integrated approach.

CRediT authorship contribution statement

Magdala Tesauro: Writing – original draft, Visualization, Validation, Software, Methodology, Investigation, Data curation, Conceptualization. **Mikhail K. Kaban:** Writing – review & editing, Writing – original draft, Validation, Software, Methodology, Investigation, Data curation, Conceptualization. **Mohammad Youssof:** Writing – review & editing, Writing – original draft, Software, Investigation, Data curation, Conceptualization.

Funding

This research did not receive any specific grant from funding agencies in the public, commercial, or not-for-profit sectors.

Declaration of competing interest

The authors declare that they have no known competing financial interests or personal relationships that could have appeared to influence the work reported in this paper.

Acknowledgments

The comments of two anonymous reviewers have greatly improved the manuscript.

Appendix A. Supplementary data

Supplementary data to this article can be found online at https://doi.org/10.1016/j.gloplacha.2026.105360.

Data availability

The velocity, thermal, and compositional models of the South African cratons displayed in the current study are available in the Zenodo repository (https://zenodo.org/uploads/18433786).

References

Adams, A., Nyblade, A., Weeraratne, D., 2012. Upper mantle shear wave velocity structure beneath the East African plateau: evidence for a deep, plateau wide low velocity anomaly. Geophys. J. Int. 189, 123–142. https://doi.org/10.1111/j.1365-246X.2012.05373.x.

Afonso, J.C., Ben-Mansour, W., O'Reilly, S., Griffin, W.L., Salajegheh, F., Foley, S., Begg, G., Selway, K., Macdonald, A., Januszczak, N., Fomin, I., Nyblade, A.A., Yang, Y., 2022. Thermochemical structure and evolution of cratonic lithosphere in central and southern Africa. Nat. Geosci. 15 (5), 1–6. https://doi.org/10.1038/s41561-022-00929-y.

Anderson, D.L., 2006. Speculations on the nature and cause of mantle heterogeneity. Tectonophysics 416 (1–4), 7–22. https://doi.org/10.1016/j.tecto.2005.07.011.

Barton, J.M., Holzer, L., Kamber, B., Doig, R., Kramers, J.D., Nyfeler, J.D., 1994. Discrete metamorphic events in the Limpopo belt, Southern Africa: implications for the application of P–T path in complex metamorphic terrains. Geology 22, 1035–1038. https://doi.org/10.1130/0091-7613(1994)022<1035:DMEITL>2.3.CO;2.

Becker, J.J., Sandwell, D.T., Smith, W.H.F., Braud, J., Binder, B., Depner, J., et al., 2009. Global bathymetry and elevation data at 30 arc seconds resolution: SRTM30_PLUS. Mar. Geod. 32 (4), 355–371. https://doi.org/10.1080/01490410903297766.

Bedle, H., Cooper, C.M., Frost, C.D., 2021. Nature versus nurture: preservation and destruction of Archean cratons. Tectonics 40, 9 e2021TC006714. https://doi.org/10.1029/2021TC006714.

Begg, G.C., Griffin, W.L., Natapov, L.M., O'Reilly, S.Y., Grand, S.P., O'Neill, C.J., Hronsky, J.M.A., Poudjom Djomani, Y., Deen, T., Bowden, P., 2009. The Lithospheric architecture of Africa. Seismic tomography, mantle petrology and tectonic evolution. Geosphere 5, 23–50. https://doi.org/10.1130/GES00179.1.

Boumann, J., Ebbing, J., Fuchs, M., Sebera, J., Lieb, V., Szwillus, W., Haagmans, R., Novak, P., 2016. Satellite gravity gradient grids for geophysics. Sci. Rep. 6, 21050. https://doi.org/10.1038/srep21050.

Boyce, A., Bastow, I.D., Cottaar, S., Kounoudis, R., Guilloud De Courbeville, J., Caunt, E., Desai, S., 2021. AFRP20: New *P*-Wavespeed Model for the African Mantle reveals two Whole-Mantle Plumes Below East Africa and Neoproterozoic Modification of the Tanzania Craton. Geochem. Geophys. Geosyst. 22, 3. https://doi.org/10.1029/2020GC009302 e2020GC009302.

Celli, N.L., Lebedev, S., Schaeffer, A.J., Gaina, C., 2020. African cratonic lithosphere carved by mantle plumes. Nature Comm. 11, 92. https://doi.org/10.1038/s41467-019-13871-2.

Cobden, L., Trampert, J., Fichtner, A., 2018. Insights on upper mantle melting, rheology, and anelastic behavior from seismic shear wave tomography. Geochem. Geophys. Geosyst. 19, 3892–3916. https://doi.org/10.1029/2017GC007370.

Connolly, J.A., 2005. Computation of phase equilibria by linear programming: a tool for geodynamic modeling and its application to subduction zone decarbonation. Earth Planet. Sci. Lett. 236 (1–2), 524–541. https://doi.org/10.1016/j.epsl.2005.04.033.

Constable, S.C., Parker, R.L., Constable, C.G., 1987. Occam's inversion: a practical algorithm for generating smooth models from electromagnetic sounding data. Geophysics 52 (3), 289–300. https://doi.org/10.1190/1.1442303.

Craig, T.J., Jackson, J.A., Priestley, K., McKenzie, D., 2011. Earthquake distribution patterns in Africa: their relationship to variations in lithospheric and geological structure, and their rheological implications. Geophys. J. Int. 185, 403–434. https://doi.org/10.1111/j.1365-246X.2011.04950.x.

Dave, R., Li, A., 2016. Destruction of the Wyoming craton: seismic evidence and geodynamic processes. Geology 44 (11). https://doi.org/10.1130/G38147.1. G38147.1.

de Wit, M.J., Roering, Ch., Hart, R.G., Armstrong, R.A., de Ronde, C.E.J., Green, R.W.E., Tredoux, M., Peberdy, E., Hart, R.A., 1992. Formation of an Archean continent. Nature 357, 553–562. https://doi.org/10.1038/357553a0.

Emry, E.L., Shen, Y., Nyblade, A.A., Flinders, A., Bao, X., 2019. Upper mantle earth structure in Africa from full-wave ambient noise tomography. Geochem. Geophys. Geosyst. 20, 120–147. https://doi.org/10.1029/2018gc007804.

Faul, U.H., Jackson, I., 2005. The seismological signature of temperature and grain size variations in the upper mantle. Earth Planet. Sci. Lett. 234 (1–2), 119–134. https://doi.org/10.1016/j.epsl.2005.02.008.

Faure, S., 2010. World kimberlites CONSOREM database (Version 3): Consortium de Recherche en Exploration Minérale CONSOREM, Université du Québec à Montréal, Numerical Database. http://www.consorem.ca.

Finger, N.-P., Kaban, M.K., Tesauro, M., Haeger, C., Mooney, W.D., Thomas, M., 2021. A thermo compositional model of the cratonic lithosphere of South America. Geochem. Geophys. Geosyst. 22. https://doi.org/10.1029/2020GC009307 e2020GC009307.

Finger, N.-P., Kaban, M.K., Tesauro, M., Mooney, W.D., Thomas, M., 2022. A thermo-compositional model of the African cratonic lithosphere. Geochem. Geophys. Geosyst. 23. https://doi.org/10.1029/2021GC010296 e2021GC010296.

Fishwick, S., 2010. Surface wave tomography: Imaging of the lithosphere–asthenosphere boundary beneath central and southern Africa. Lithos 120 (1–2), 63–73. https://doi.org/10.1016/j.lithos.2010.05.011.

Förste, C., Bruinsma, S.L., Abrikosov, O., Lemoine, J.-M., Marty, J.C., Flechtner, F., Balmino, G., Barthelmes, F., Biancale, R., 2014. EIGEN-6C4 the latest combined global gravity field model including GOCE data up to degree and order 2190 of GFZ Potsdam and GRGS Toulouse. GFZ Data Services. https://doi.org/10.5880/ICGEM.2015.1.

Griffin, W.L., O'Reilly, S.Y., Natapova, L.M., Ryan, C.G., 2003. The evolution of lithospheric mantle beneath the Kalahari Craton and its margins. Lithos 71, 215–241. https://doi.org/10.1016/j.lithos.2003.07.006.

Fouch, M.J., James, D.E., VanDecar, J.C., van der Lee, S., 2004. Mantle seismic structure beneath the Kaapvaal and Zimbabwe Cratons. S. Afr. J. Geol. 107 (1–2), 33–44.

Griffin, W.L., Grahama, S., O'Reilly, S.Y., Pearson, N.J., 2004. Lithosphere evolution beneath the Kaapvaal Craton: Re–Os systematics of sulfides in mantle-derived peridotites. Chem. Geol. 208 (1), 89–118. https://doi.org/10.1016/j.chemgeo.2004.04.007.

Hoal, K.E.O., 2003. Samples of Proterozoic Fe-enriched mantle form the Premier kimberlite. Lithos 71, 259–272. https://doi.org/10.1016/S0024-4937(03)00116-6.

James, D.E., Niub, F., Rokosk, J., 2003. Crustal structure of the Kaapvaal craton and its significance for early crustal evolution. Lithos 71, 413–429. https://doi.org/10.1016/j.lithos.2003.07.009.

Jelsma, H.A., Dirks, P.H.G., 2002. Neoarchaean tectonic evolution of the Zimbabwe Craton. Geol. Soc. London Spec. Publ. 199 (1), 183–211. https://doi.org/10.1144/GSL.SP.2002.199.01.10.

Jordan, T.H., 1978. Composition and development of the continental tectosphere. Nature 274, 544–548. https://doi.org/10.1038/274544a0.

Kaban, M.K., Petrunin, A.G., Schmeling, H., Shahraki, M., 2014a. Effect of decoupling of lithospheric plates on the observed geoid. Surv. Geophys. https://doi.org/10.1007/s10712-014-9281-3.

Kaban, M.K., Tesauro, M., Mooney, W.D., Cloetingh, S.A.P.L., 2014b. Density, temperature and composition of the North American lithosphere—New insights form a joint analysis of seismic, gravity and mineral physics data: 1. Density structure of the crust and upper mantle. Geophys. Geochem. Geosyst. 15, 12, 4781–4807. https://doi.org/10.1002/2014GC005483.

Kaban, M.K., Mooney, W.D., Petrunin, A.G., 2015. Cratonic root beneath North America shifted by basal drag from the convecting mantle. Nat. Geosci. 8, 797–800. https://doi.org/10.1038/ngeo2525.

Kaban, M.K., Stolk, W., Tesauro, M., El Khrepy, S., Al-Arifi, N., Beekman, F., Cloetingh, S. A.P.L., 2016a. 3D density model of the upper mantle of Asia based on inversion of gravity and seismic tomography data. Geochem. Geophys. Geosyst. 17. https://doi.org/10.1002/2016GC006458.

Kaban, M.K., El Khrepy, S., Al-Arifi, N., 2016b. Isostatic Model and Isostatic Gravity Anomalies of the Arabian Plate and Surroundings. Pure Appl. Geophys. 173 (4), 1211–1221. https://doi.org/10.1007/s00024-015-1164-0.

Kaban, M.K., Sidorov, R.V., Soloviev, A.A., Gvishiani, A.D., Petrunin, A.G., Petrov, O.V., Kashubin, S.N., Androsov, E.A., Milshtein, E.D., 2022. A New moho map for North-Eastern Eurasia based on the analysis of various geophysical data. Pure Appl. Geophys. 179 (1), 1–14. https://doi.org/10.1007/s00024-021-02925-6.

Kachingwe, M., Nyblade, A., Julià, J., 2015. Crustal structure of Precambrian terranes in the southern African subcontinent with implications for secular variation in crustal genesis. Geophys. J. Int. 202, 533–547. https://doi.org/10.1093/gji/ggv136.

Karato, S.I., 1993. Importance of anelasticity in the interpretation of seismic tomography. Geophys. Res. Lett. 20 (15), 762, 1623–1626. https://doi.org/10.1029/93GL01767.

Karato, S.I., Jung, H., 1998. Water, partial melting and the origin of the seismic low velocity and high attenuation zone in the upper mantle. Earth Planet. Sci. Lett. 157 (3–4), 193–207. https://doi.org/10.1016/S0012-821X(98)00034-X.

Kobussen, A.F., Griffin, W.L., O'Reilly, S.Y., 2009. Cretaceous thermo-chemical modification of the Kaapvaal cratonic lithosphere, South Africa. Lithos 112, 886–895. https://doi.org/10.1016/j.lithos.2009.06.031.

Kusky, T.M., Brian, F., Windley, B.F., Wang, L., Wang, Z., Li, X., Zhu, P., 2014. Flat slab subduction, trench suction, and craton destruction: comparison of the North China, Wyoming, and Brazilian cratons. Tectonophysics 630, 208–221. https://doi.org/10.1016/j.tecto.2014.05.028.

Lee, C.-T.A., Luffi, P., Chin, E.J., 2011. Building and Destroying Continental Mantle. Annu. Rev. Earth Planet. Sci. 39, 59–90. https://doi.org/10.1146/annurev-earth-040610-133505.

Legendre, C.P., Meier, T., Lebedev, S., Friederich, W., Viereck-Götte, L.A., 2012. Shear wave velocity model of the European upper mantle from automated inversion of seismic shear and surface waveforms. Geophys. J. Int. 191, 282–304. https://doi.org/10.1111/j.1365-246X.2012.05613.x.

Matthews, P.E., 1981. Eastern or Natal sector of the Namaqua–Natal Movile Belt in southern Africa. In: Hunter, D.R. (Ed.), Precambrian of the Southern Hemisphere. Elsevier, Amsterdam, pp. 705–725.

Mazzotti, S., 2007. Geodynamic models for earthquake studies in intraplate North America. In: Stein, S., Mazzotti, S. (Eds.), Continental Intraplate Earthquakes: Science, Hazard, and Policy Issues, 425. Geol. Soc. Am. Spec. Pap., pp. 17–33. https://doi.org/10.1130/2007.2425(02

McDonough, W.F., Sun, S.-S., 1995. The composition of the Earth. Chem. Geol. 120, 223–253. https://doi.org/10.1016/0009-2541(94)00140-4.

Meibom, A., Anderson, D.L., Sleep, N.H., Frei, R., Chamberlain, C.P., Hren, M.T., Wooden, J.L., 2003. Are high $^{3}He/^{4}He$ ratios in oceanic basalts an indicator of deep-mantle plume components? Earth Planet. Sci. Lett. 208 (3–4), 197–204. https://doi.org/10.1016/S0012-821X(03)00038-4.

Mooney, W., 2007. Crust and Lithospheric Structure – Global Crustal Structure. Treatise on Geophysics 1, 361–417. https://doi.org/10.1016/B978-044452748-6.00011-0.

Mooney, W.D., 2015. Crust and lithospheric structure—Global crustal structure. In: Schubert, G., Romanowicz, B., Dziewonski, A. (Eds.), Treatise on Geophysics, 2nd ed. Elsevier, pp. 339–390. https://doi.org/10.1016/B978-0-444-53802-4.00010-5.

Pasyanos, M.E., Nyblade, A.A., 2007. A top to bottom lithospheric study of Africa and Arabia. Tectonophysics 444 (1–4), 27–44. ISSN 0040-1951. https://doi.org/10.1016/j.tecto.2007.07.008.

Priestley, K., Debayle, E., McKenzie, D., Pilidou, S., 2006. Upper mantle structure of eastern Asia from multimodesurface waveform tomography. J. Geophys. Res. 111, B10304. https://doi.org/10.1029/2005JB004082.

Root, B.C., Novák, P., Dirkx, D., Kaban, M.K., van der Wal, W., Vermeersen, L.L.A., 2016. On a spectral method for forward gravity field modelling. J. Geodyn. 97, 22–30. https://doi.org/10.1016/J.JOG.2016.02.008.

Schaeffer, A.J., Lebedev, S., 2013. Global shear-speed structure of the upper mantle and transition zone. Geophys. J. Int. 194 (1), 417–449. https://doi.org/10.1093/gji/ggt095.

Sebai, A., Stutzmann, E., Montagner, J.P., Sicilia, D., Beucler, E., 2006. Anisotropic structure of the African upper mantle from Rayleigh and love wave tomography. Phys. Earth Planet. Inter. 155 (1–2), 48–62. https://doi.org/10.1016/j.pepi.2005.09.009.

Simon, N.S.C., Irvine, G.J., Davies, G.R., Pearson, D.G., Carlson, R.W., 2003. The origin of garnet and clinopyroxene in "depleted" Kaapvaal peridotites. Lithos 71 (2–4), 289–322. https://doi.org/10.1016/S0024-4937(03)00118-X.

Sloan, R.A., Jackson, J.A., McKenzie, D., Priestley, K., 2011. Earthquake depth distributions in Central Asia, and their relations with litho sphere thickness, shortening and extension. Geophys. J. Int. 185, 1–29. https://doi.org/10.1111/j.1365-246X.2010.04882.x.

Snyder, D.B., Humphreys, E., Pearson, D.G., 2017. Construction and destruction of some north American cratons. Tectonophysics 694, 464–485. https://doi.org/10.1016/j.tecto.2016.11.032.

Sobolev, S.V., Sobolev, A.V., Kuzmin, D.V., Krivolutskaya, N.A., Petrunin, A.G., Arndt, N. T., Radko, V.A., Vasiliev, Y.R., 2011. Linking mantle plumes, large igneous provinces and environmental catastrophes. Nature 477, 312–316. https://doi.org/10.1038/nature10385.

Sodoudi, F., Yuan, X., Kind, R., Lebedev, S., Adam, J.M.-C., Kastle, E., Tilmann, F., 2013. Seismic evidence for stratification in composition and anisotropic fabric within the thick lithosphere of Kalahari Craton. Geochem. Geophys. Geosyst. 14. https://doi.org/10.1002/2013GC004955.

Sodoudi, F., Kind, R., Hatzfeld, D., Priestley, K., Hanka, W., Wylegalla, K., Stavrakakis, G., Vafidis, A., Harjes, H.-P., Bohnhoff, M., 2006. Lithospheric structure of the Aegean obtained from P and S receiver functions. J. Geophys. Res. 111, B12307. https://doi.org/10.1029/2005JB003932.

Stixrude, L., Lithgow-Bertelloni, C., 2022. Thermal expansivity, heat capacity and bulk modulus of the mantle. Geophys. J. Int. 228, 1119–1149. https://doi.org/10.1093/gji/ggab394.

Tappe, S., Smarta, K., Torsvik, T., Massuyeaua, M., de Wit, M., 2018. Geodynamics of kimberlites on a cooling Earth: Clues to plate tectonic evolution and deep volatile cycles. Earth Planet. Sci. Lett. 484, 1–14. https://doi.org/10.1016/j.epsl.2017.12.013.

Tesauro, M., Kaban, M.K., Mooney, W.D., Cloetingh, S.A.P.L., 2014. Density, temperature, and composition of the north American lithosphere—New insights from a joint analysis of seismic, gravity, and mineral physics data: 2. Thermal and compositional model of the upper mantle. Geochem. Geophys. Geosyst. 15. https://doi.org/10.1002/2014GC005484.

Tesauro, M., Kaban, M.K., Aitken, A.R.A., 2020. Thermal and compositional anomalies of the Australian upper mantle from seismic and gravity data. Geochem. Geophys. Geosyst. 21. https://doi.org/10.1029/2020GC009305 e2020GC009305.

van Herwaarden, D.-P., Thrastarson, S., Hapla, V., Afanasiev, M., Trampert, J., Fichtner, A., 2023. Full-waveform tomography of the African Plate using dynamic mini-batches. J. Geophys. Res. Solid Earth 128. https://doi.org/10.1029/2022JB026023 e2022JB026023.

Wang, H., Van Hunen, J., Pearson, D.G., 2015. The thinning of subcontinental lithosphere: the roles of plume impact and metasomatic weakening. Geochem. Geophys. Geosyst. 18, 1541–1576. https://doi.org/10.1002/2015GC005784.

Weeraratne, D.S., Forsyth, D.W., Fischer, K.M., Nyblade, A.A., 2003. Evidence for an upper mantle plume beneath the Tanzanian craton from Rayleigh wave tomography. J. Geophys. Res. 108 (B9), 2427. https://doi.org/10.1029/2002JB002273.

Wittlinger, G., Farra, V., 2007. Converted waves reveal a thick and layered tectosphere beneath the Kalahari super-craton. Earth Planet. Sci. Lett. 254, 404–415. https://doi.org/10.1016/j.epsl.2006.11.048.

Wu, F.-Y., Yang, J.H., Xu, Y.-G., Wilde, S.A., Walker, R., 2019. Destruction of the North China Craton in the Mesozoic. Annu. Rev. Earth Planet. Sci. 47, 173–195. https://doi.org/10.1146/annurev-earth-053018-060342.

Youssof, M., Thybo, H., Artemieva, I.M., Levander, A., 2013. Moho depth and crustal composition in Southern Africa. Tectonophysics 609, 267–287. https://doi.org/10.1016/j.tecto.2013.09.001.

Youssof, M., Thybo, H., Artemieva, I.M., Levander, A., 2015. Upper mantle structure beneath southern African cratons from seismic finite-frequency P- and S-body wave tomography. Earth Planet. Sci. Lett. 420, 174–186. https://doi.org/10.1016/j.epsl.2015.01.034.

Zhang, W., Jiménez-Munt, I., Torne, M., Vergés, J., Bravo-Gutiérrez, E., Negredo, A.M., García-Castellanos, D., 2024. The lithosphere and upper mantle of the Western-Central Mediterranean region from integrated geophysical-geochemical modeling. J. Geophys. Res. Solid Earth 129. https://doi.org/10.1029/2023JB028435 e2023JB028435.

Zhu, R.X., Zheng, T.Y., 2009. Destruction geodynamics of the North China Craton and its Paleoproterozoic plate tectonics. Chin. Sci. Bull. 2009 (54), 3354–3366. https://doi.org/10.1007/s11434-009-0451-5.